Numerically exact calculation of electromagnetic heat transfer between a dielectric sphere and plate

Clayton Otey[1] and Shanhui Fan[2]

[1]*Department of Applied Physics, Stanford University, Stanford, California 94305, USA*
[2]*Department of Electrical Engineering, Stanford University, Stanford, California 94305, USA*

We present a numerically exact calculation of electromagnetic heat transfer between a dielectric sphere and plate. We compare the calculation to a recent experiment. Our calculations unify various approximations previously used to treat this problem, and provide a basis for new physical insights into the design of nanoscale thermal transfer experiments.

PACS number(s): 44.05.+e, 44.40.+a, 45.10.−b, 05.40.−a

I. INTRODUCTION

Near-field electromagnetic heat transfer holds great potential for the advancement of nanotechnology. Whereas far-field electromagnetic heat transfer is constrained by Planck's blackbody limit, the increased density of states in the near field enhances heat transfer rates by orders of magnitude relative to the conventional far-field limit.[1–3] Such enhancement opens up new possibilities in numerous applications,[4] including thermal photovoltaics,[5] nanopatterning,[6] high-resolution material surface probing and imaging,[7–10] and thermally assisted magnetic recording.[11] The advancement in this area was hampered by the lack of rigorous theoretical treatment for geometries that are of direct experimental relevance, such as the sphere-plate geometry.[12–14] Recently, at least two groups have theoretically addressed the sphere-plate electromagnetic heat transfer problem[15,16] using a variation on a mode-based scattering theory approach.[17,18] This approach is closely related to computations of Casimir observables in similar geometries.[19,20]

Here we expand upon Ref. 16, and present in detail our numerically exact calculations of the electromagnetic heat flux between a sphere [with a spatially homogenous dielectric function $\varepsilon_A(\omega)$, a radius a, at a temperature T_A] and a plate [assumed to fill a half space, with a spatially homogenous dielectric function $\varepsilon_B(\omega)$, at temperature T_B], separated by a vacuum gap (with $\varepsilon = 1$, and a gap distance d). By numerically exact, we mean that the results of our calculations should converge to exact results, as we increase the number of basis functions used to describe the fields. We consider the nonequilibrium situation where the sphere and the plate are maintained at different temperatures, T_A and T_B, respectively. A schematic rendering of the geometrical configuration is shown in Fig. 1.

The paper is organized as follows: In Sec. II we will describe the computational method. Some numerical implementation details, in particular those that allow us to efficiently calculate the heat flux in extreme geometries, are outlined in Sec. III. Section IV A contains a detailed comparison with experimental datafrom Ref. 14. Section IV B contains some comparisons between our numerically exact fluctuational electrodynamics calculation and various physically intuitive approximations: the far-field limit, the dipole limit, and the proximity approximation.

II. COMPUTATIONAL METHOD

A general scattering approach to this problem, which allows for an arbitrary number of bodies, in principle, has been described before.[15] Here we present a concise derivation of the scattering formulation in the present sphere-plate case, with a specific focus on those aspects that pertain to our computation. The underlying physical assumptions are those of fluctuational electrodynamics of Rytov,[21,22] and notation is borrowed from various related work.[15–17,23]

First, regarding notation, all repeated indices are implicitly summed over, unless they appear on both sides. Now, consider first the outgoing thermal radiation from an isolated sphere maintained at a constant temperature T_A. The electric field of this radiation outside the sphere can be expanded as $\mathbf{E}^0(\vec{r}) = A^0_{\alpha_+}\Psi_{\alpha_+}(\vec{r})$ in a complete basis Ψ_{α_+} of outgoing solutions to the free-space Maxwell equation

$$\left(-\frac{\omega^2}{c^2}\mathbb{I} + \nabla \times \nabla \times\right)\Psi_{\alpha_+}(\vec{r}) = 0. \tag{1}$$

We use $\alpha = \{l,m,P,S\}$ as a multi-index specifying the vector spherical harmonics defined with respect to the center of the sphere. Here l is the total angular momentum, m is the angular momentum component along the z direction, P labels the polarization, and $S \in \{+,0,-\}$ labels the type of solution, in the sense of outgoing $(+)$, regular (0), or incoming $(-)$ waves. In the following, we use α_S to denote an index into the vector spherical harmonic basis, restricted to a particular type of wave, so for example, α_0 is an index into regular spherical waves. Notice that the α_S index is independent of the α index. Primed indices α'_S refer to the same basis as α_S, and are used when one such index does not suffice.

The thermal sources in the sphere are correlated according to the fluctuation-dissipation theorem, resulting in a correlation of electric fields,[15,24]

$$\langle \mathbf{E}^0(\vec{r}) \otimes \mathbf{E}^{0*}(\vec{r}')\rangle \equiv \mathbb{D}^0_{\alpha\alpha'}\Psi_\alpha(\vec{r}) \otimes \Psi^*_{\alpha'}(\vec{r}'), \tag{2}$$

where the unperturbed correlator $\mathbb{D}^0_{\alpha\alpha'} = \langle A^0_\alpha A^{0*}_{\alpha'}\rangle\delta_{\alpha\alpha'}\delta_S$. The temperature dependence can be extracted as $\mathbb{D}^0_{\alpha\alpha'} = \tilde{\mathbb{D}}^0_{\alpha\alpha'}\Theta(\omega,T)$, where $\Theta(\omega,T) = \hbar\omega/[\exp(\hbar\omega/k_BT) - 1]$ is the mean thermal energy of each mode due to its occupation by thermal photons.

We now introduce the plate. Here as a starting point we assume that the plate is at zero temperature, and thus the thermal radiation originates entirely from the sources in the sphere. We define a basis of cylindrical waves $\Phi_\beta(\vec{r})$, with origin at the point on the plate closest to the sphere; the $\hat{z}$ axis is directed from this origin to the center of the sphere. The indices in this case are $\beta = \{\lambda,m,h,P,S\}$, where λ is the cylindrical
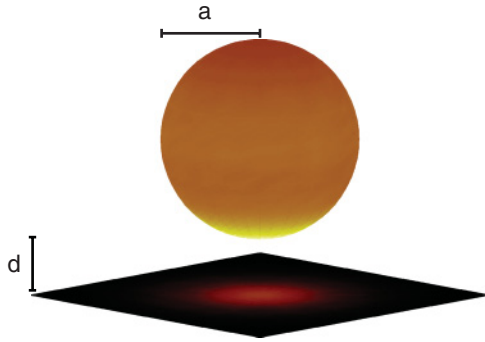
FIG. 1. (Color online) A schematic of the geometry considered: a dielectric sphere of radius a, and a dielectric plate separated by a distance d through a vacuum gap. The color corresponds to electric-field intensity near the surface of the sphere and the plate, using the parameters $a = 1000$ nm and $d = 800$ nm as a representative example. The field near the sphere is much greater than that near the plate, so in order to resolve the variation in intensity, the scales (see the color bars on the right) are not the same. In all the examples in this paper, the sphere and plate are both amorphous SiO_2, the sphere is at temperature $T_1 = 321$ K, and the plate is at $T_2 = 300$ K.

radial wave number, h is the wave number in the axial $\hat{z}$ direction, P is the polarization, and $S \in \{+, -\}$ with "+" referring to outgoing waves propagating away from the plate toward the sphere, and "−" referring to incoming cylindrical plane waves, respectively. Both incoming and outgoing waves in this case are regular in the radial direction.

When the plate is introduced, the total radiated field from the sphere is now $\mathbf{E}(\vec{r})$, which can be expanded on the cylindrical wave basis as $\mathbf{E}(\vec{r}) = B_\beta \Phi_\beta(\vec{r})$. The correlation function of the radiated field is then

$$\langle \mathbf{E}(\vec{r}) \otimes \mathbf{E}^*(\vec{r}') \rangle \equiv \mathbb{D}_{\beta\beta'} \Phi_\beta(\vec{r}) \otimes \Phi_{\beta'}^*(\vec{r}'), \quad (3)$$

where $\mathbb{D}_{\beta\beta'} = \langle B_\beta B_{\beta'}^* \rangle$. Moreover, defining $B_\beta = \mathbb{O}_{\beta\alpha'_+} A_{\alpha'_+}^0$, where $\mathbb{O}_{\beta\alpha_-}$ describes the scattering (by the plate) of waves emitted from the sphere, we have

$$\mathbb{D}_{\beta\beta'} = \mathbb{D}_{\beta\alpha_+} \mathbb{D}_{\alpha_+\alpha'_+}^0 (\mathbb{O}_{\beta'\alpha'_+})^\dagger. \quad (4)$$

To determine $\mathbb{O}_{\beta\alpha_+}$, we consider the resulting total electric field $\mathbf{E}^\alpha$ that is consistent with a wave incident on the plate from the sphere Ψ_{α_+}. We expand $\mathbf{E}^\alpha$ in the vacuum region in terms of outgoing spherical waves from the sphere, and outgoing cylindrical waves from the plate,

$$\mathbf{E}^\alpha = A_{\alpha_+}^\alpha \Psi_{\alpha_+} + B_{\beta_+}^\alpha \Phi_{\beta_+}. \quad (5)$$

It is now useful to introduce the operators $\Lambda_{\alpha_0\beta_+}$ and $\Lambda_{\beta_-\alpha_+}$, which relate the vector spherical and cylindrical waves. The operator $\Lambda_{\alpha_0\beta_+}$ transforms a cylindrical wave, labeled by β_+, into a spherical wave labeled by α_0. Likewise, the operator $\Lambda_{\beta_-\alpha_+}$ transforms a spherical wave labeled by α_+ into a cylindrical wave labeled by β_-. Integral expressions for these operators exist in the literature.[25] The only source of cylindrical waves is the reflection of spherical waves from the plate, so

$$B_{\beta_+}^\alpha = R_{\beta_+\beta_-} \Lambda_{\beta_-\alpha_+} A_{\alpha_+}^\alpha, \quad (6)$$

where $R_{\beta_+\beta_-}$ are the reflection coefficients for the cylindrical plane waves at the plate surface. The outgoing spherical

waves originate from both the sources in the sphere, and from reflection of cylindrical waves by the sphere, so

$$A_{\alpha_+}^\alpha = A_{\alpha_+}^0 \delta_{\alpha_+\alpha} + R_{\alpha_+\alpha_0} \Lambda_{\alpha_0\beta_+} B_{\beta_+}^\alpha, \quad (7)$$

where $R_{\alpha_+\alpha_0}$'s are the Mie reflection coefficients for the spherical waves at the boundary of the sphere [note that following our convention, α_+ is not summed over in Eq. (7)]. Simple analytic expressions for $A_{\alpha_+}^0$ can be derived from computations of thermal radiation from an isolated sphere using the fluctuation-dissipation theorem, and are found in the literature.[23] We provide formulas for R, Λ, and A in the Appendix.

Combining Eqs. (6) and (7), we have

$$(\delta_{\alpha_+\alpha'_+} - T_{\alpha_+\alpha'_+}) A_{\alpha'_+}^\alpha = A_{\alpha'_+}^0 \delta_{\alpha_+\alpha}, \quad (8)$$

where we have defined $T_{\alpha_+\alpha'_+} \equiv R_{\alpha_+\alpha_0} \Lambda_{\alpha_0\beta_+} R_{\beta_+\beta_-} \Lambda_{\beta_+\alpha'_+}$. Having determined $A_{\alpha_+}^\alpha$ using Eq. (8), we can transform the field to the complete β basis,

$$\mathbb{O}_{\beta\alpha_+} = T_{\beta_+\beta_-} \Lambda_{\beta_-\alpha'_+} (\delta_{\alpha_-\alpha'_+} - T_{\alpha_+\alpha'_+})^{-1}, \quad (9)$$

where $T_{\beta_+\beta_-}$ are the transmission coefficients for cylindrical plane waves incident on the plate.

We can now calculate the energy flux from the sphere to the plate through a plane in the vacuum region, with the sphere at a temperature T, and the plate at a temperature of 0 K. It is convenient to introduce the following operator, related to the Poynting vector,

$$\mathbb{S}_{\beta\beta'}(\omega) = \text{Re} \frac{i}{\omega\mu_0} \int_{\partial V_{\text{plate}}} \mathbf{dn} \cdot \{\Phi_\beta(\omega) \times [\nabla \times \Phi_{\beta'}(\omega)]^*\}. \quad (10)$$

Then we can write the energy flux

$$\begin{aligned} S(\omega, T) &= \text{Re} \frac{i}{\omega\mu_0} \int_{\partial V_{\text{plate}}} \mathbf{dn} \cdot \langle \mathbf{E}(\omega) \times [\nabla \times \mathbf{E}(\omega)]^* \rangle_T \\ &= \mathbb{S}_{\beta\beta'} \mathbb{D}_{\beta\beta'} = \mathbf{Tr}[\mathbb{S}\mathbb{D}] = \mathbf{Tr}[\mathbb{S}\mathbb{O}\mathbb{D}^0\mathbb{O}^\dagger] \\ &= (\mathbb{O}_{\beta'\alpha'_+})^\dagger \mathbb{S}_{\beta\beta'} \mathbb{O}_{\beta'\alpha_+} \tilde{\mathbb{D}}_{\alpha_+\alpha'_+}^0 \Theta(\omega, T) \\ &= S_{\alpha'_+\alpha''_+} A_{\alpha'_+}^{\alpha*} A_{\alpha''_+}^\alpha, \end{aligned} \quad (11)$$

where we have introduced

$$S_{\alpha_+\alpha'_-} \equiv (\Lambda_{\beta'_-\alpha_+})^\dagger (T_{\beta'_+\beta'_-})^\dagger \mathbb{S}_{\beta'_-\beta_-} T_{\beta_+\beta_-} \Lambda_{\beta_-\alpha'_+}. \quad (12)$$

Finally, we wish to determine the heat transfer in the nonequilibrium case, where the sphere is at a temperature T_A, and the plate is at a temperature T_B. Using a reciprocity argument,[1] the net heat transfer can be written as

$$\begin{aligned} Q(T_A, T_B) &= Q(T_A, 0) + Q(0, T_B) \\ &= \int_0^\infty d\omega [S(\omega, T_A) - S(\omega, T_B)]. \end{aligned} \quad (13)$$

III. NUMERICAL DETAILS AND CONVERGENCE

In this section we provide numerical details on the implementation of the computational method described in the previous section.

When carrying out the frequency integration of $S(\omega, T)$ in Eq. (13), we sample the frequency space by explicitly choosing

a few dozen frequencies, which suffices to resolve the relevant dielectric resonances around the thermal wavelength.

To calculate the heat flux spectral density $S(\omega, T)$ at a given frequency, we can decompose the flux as $Q = \sum_{m=0}^{m_{max}} \sum_{l=l_{min}}^{l_{max}} Q(m, l)$, where $Q(m, l) = S_{\alpha'_+ \alpha''_+} A^{\alpha_{lm}*}_{\alpha'_+} A^{\alpha_{lm}}_{\alpha''_+}$, as in Eq. (11), but with α now restricted to a given α_{lm}. In the numerical calculation of $Q(m, l)$, l ranges between $l_{min} = \max(1, m)$ and a heuristically determined l_{max}. The choice of l_{max} will be discussed in detail in the convergence analysis.

The calculation proceeds in two steps: (1) solving for the spherical scattering coefficients $A^{\alpha_{lm}}_{\alpha+vm}$, using Eq. (8) and (2) calculating the flux contributions given these spherical scattering coefficients, using Eq. (12).

In step (1), Eq. (8) becomes a dense linear system in a $N = 2(l_{max} - l_{min} + 1)$ dimensional vector space [note that since $l_{min} = \max(1, m)$, N varies with m]. In setting up the matrix on the left-hand side of Eq. (8), we use adaptive Gauss-Kronrod numerical quadrature[26] to perform the integration over the cylindrical radial wave number $\lambda \in \beta$. Notice that λ is a continuous variable. There are N^2 such numerical quadrature in the calculation of $T_{\alpha\alpha'}$. In practice we do not perform all N^2 integrations; we use a heuristic numerical condition to determine if the value should negligibly differ from 0. In step (2), we similarly perform $\propto N^2$ numerical integrations to calculate $S_{\alpha\alpha'}$. Note that the cylindrical β coordinates (in particular the continuous λ) show up only in inner loops in the final form for the heat flux in Eq. (12).

We now provide a brief physically motivated convergence analysis. Our expectation is that reasonable convergence should be achieved when l_{max} is large enough to resolve the relevant spatial scales. In general, the far-field contributions require $l_{max} \propto (a\omega/c)$, and the near-field contributions require $l_{max} \propto a/d$, as in Ref. 23. In our implementation we set

$$l_{max} = \kappa_0 + \kappa_1(a\omega/c) + \kappa_2(a/d). \quad (14)$$

We typically set $\kappa_0 = 8$, $\kappa_1 = 2.5$, and $\kappa_2 = 1.0$.

To demonstrate the convergence behavior, as a specific example, we consider a system with $a = 20$ μm and $d = 100$ nm, with the sphere maintained at $T_A = 321$ K and the plate at $T_B = 300$ K. Both the sphere and plate are silica glass; we use the dielectric function taken from Ref. 27. This example corresponds to one of the structures measured in Ref. 14. For this example, in Fig. 2, we plot $Q(m)$ and $Q(l)$, defined as

$$Q(m) = \sum_l Q(m, l),$$
$$Q(l) = \sum_m Q(m, l), \quad (15)$$

as a function of m and l, respectively. We see that $Q(l)$ decays as a function of l. To reach a 1% convergence, we require $l_{max} \gtrsim 700$. Hence, Eq. (8) represents a modestly sized linear system, even in such an extreme geometry with $a/d = 200$.

We have found similar convergence behavior as in Fig. 2 in all numerical data that we have presented in this paper. If we vary κ_1 (or κ_2) by 20%, then the results change by less than 2%. We find that the error decays exponentially as a function of κ_1, κ_2 for $\kappa_1 \gtrsim 2.0$, $\kappa_2 \gtrsim 0.8$.

Our implementation for the sphere-plate configuration can accurately and efficiently handle even more extreme geometric
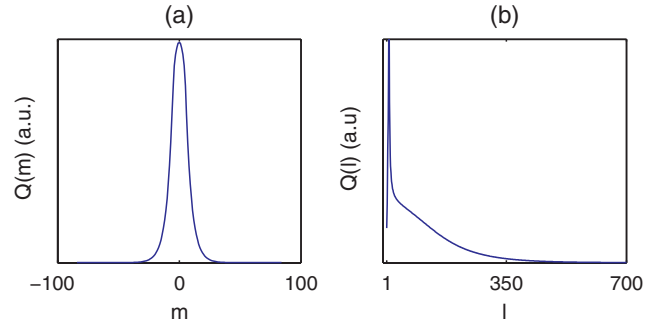

FIG. 2. (Color online) Typical contribution to the spectral energy flux as a function of m and l [$a = 20$ μm, $d = 100$ nm, $\hbar\omega = 0.0605$ eV(corresponding to a surface phonon polariton resonance), $\varepsilon_1 = \varepsilon_2$ corresponds to amorphous SiO$_2$].

configurations, such as those seen in experiments where $a/d \gtrsim 10^3$. In order to efficiently achieve a large l_{max}, we find it necessary to (1) use 128-bit precision floating point arithmetic; (2) make use of message passing interfaces (MPI) and parallel computation [we have utilized 32 8-core processors from the National Center for Scientific Applications (NCSA) at University of Illinois]; and (3) implement a coupled, normalized calculation of appropriately scaled Bessel and Legendre functions of higher orders. The source code that implements all these aspects can be found online.[28]

IV. RESULTS

In this section, we compare our numerical calculations with experiments, and with various approximations commonly used to describe thermal transfer in the sphere-plate geometry. We show that our calculations are consistent with experiments. Our calculations also provide a unified view of various approximations.

A. Comparison to experimental data

We directly compare our results with the experimental sphere-plate heat flux data from Ref. 14. The data in this experiment were taken with $T_1 = 321$ K, $T_2 = 300$ K, $a = 20$ μm, and 20 nm $< d < 3$ μm. For reference, the thermal wavelength $\lambda_T \equiv hc/k_B T$ as well as the electromagnetic surface resonance wavelengths for silica surfaces are on the order of 10 μm.

In the experiment described in Ref. 14, a silica sphere is attached to a cantilever. The deformation $\Delta(d)$ of the cantilever is then measured as the sphere is moved in the vicinity of a silica plate, where d is the sphere-plate vacuum gap. The heat flux between the sphere and plate is related to the deformation as

$$Q(d) - Q(d \rightarrow \infty) = H\Delta(d - d_0). \quad (16)$$

H and d_0 are experimental calibration parameters. Measurements of similar cantilevers suggested $H = 2.30 \pm 0.69$ nW/nm. The characteristic surface roughness was 40 nm, and hence there is uncertainty in d_0 as well.[14] In comparing theoretical calculations of $Q(d)$ with such experiments, we note that the experiments do not directly measure $Q(d \rightarrow \infty)$, i.e., the far-field contribution was not directly measured.
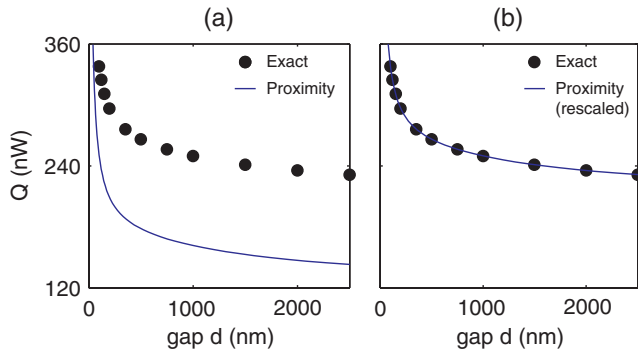
FIG. 3. (Color online) A comparison of our numerical results to the experiments in Ref. 14. (a) Our results do not agree with the proximity approximation. (b) The proximity approximation (and the experimental data from Ref. 14) can be scaled to match our results.

Based on their experimental $\Delta(d)$ data,[14] Greffet *et al.* reported an excellent fit of the proximity approximation to $Q(d)$, using the parameters $Q(d \to \infty) = 5.45$ nW, $H = 2.162$ nW/nm, and $d_0 = 31.8$ nm. Our numerically exact results of $Q(d)$ do not agree with the proximity approximation, as seen in Fig. 3(a). However, as seen Fig. 3(b), our results for $Q(d)$ can be fit to the experimental $\Delta(d)$ data as well, with the choice of parameters $Q(d \to \infty) = 9.74$ nW, $H = 2.134$ nW/nm, and $d_0 = 32.3$ nm. We note that the differences
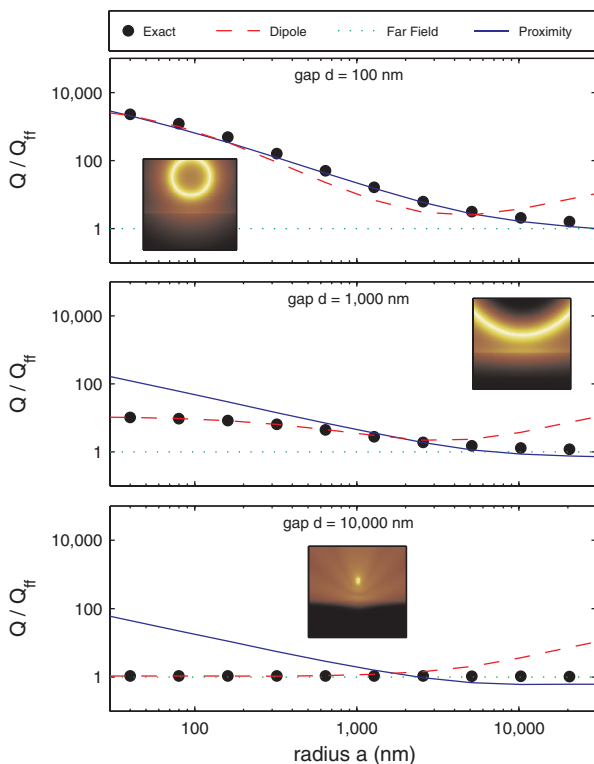

FIG. 4. (Color online) Heat flux as a function of a for fixed $d = 100$ nm, 1 μm, and 10 μm. Insets are calculated scattered electric-field intensities (located in the figure at the appropriate value of a,d). Each curve is normalized by the far-field heat flux Q_{ff}, which is by definition independent of d.
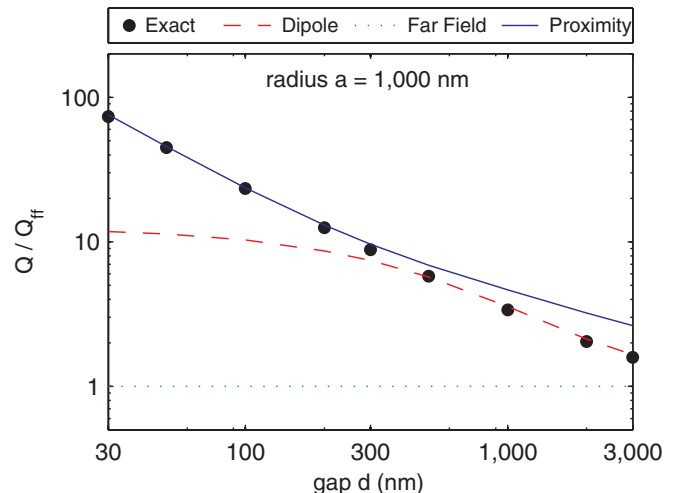

FIG. 5. (Color online) Numerically exact heat flux compared with dipole and proximity approximations, as a function of d, with fixed $a = 1$ μm.

between these two sets of parameters are well within experimental uncertainties. The fact that the same experimental data can be fit to two very different theoretical models should motivate a more thorough assessment of uncertainties in precision nanoscale sphere-plate electromagnetic heat transfer experiments.

B. Comparison to various approximations

There have been a large number of works treating this problem with a variety of approximations.[12–14,29–32] Many of these approximations were not directly tested against experiment. Only the far-field limit and the so-called "proximity approximation"[14,33] were used to fit experimental nanoscale heat transfer data.[12–14] In particular, a recent work has emphasized that the far-field contribution, which can be significant in the sphere-plate geometry, is not treated correctly in the standard proximity approximation.[32] We find that these approximations tend to break down in regimes that are of practical interest for experimental probing of nanoscale heat transfer. Thus, a careful comparison of these approximations with the numerically exact calculation can provide physical insight, which may be useful in designing experiments.

To this end, we explore a wide $a - d$ parameter space using our method. In Fig. 4 we plot the numerically exact heat flux Q as a function of sphere radius a, for various fixed gap distances d. We compare our results with three commonly used approximations in order to provide a unifying picture across different regimes.

Far-field approximation. In Fig. 4, we normalize the values for the heat flux to the far-field approximation Q_{ff}, which we define as the heat flux in the absence of interference due to secondary reflection from the sphere. In particular, it ignores near-field effects and geometrical effects that are not captured in the angular distribution of far-field radiation. We calculate this limit as follows: First, we calculate the isotropic far-field radiation from the sphere in the absence of the plate, as well as the angle-dependent absorption for incident plane waves for the plate. The far-field approximation is then determined
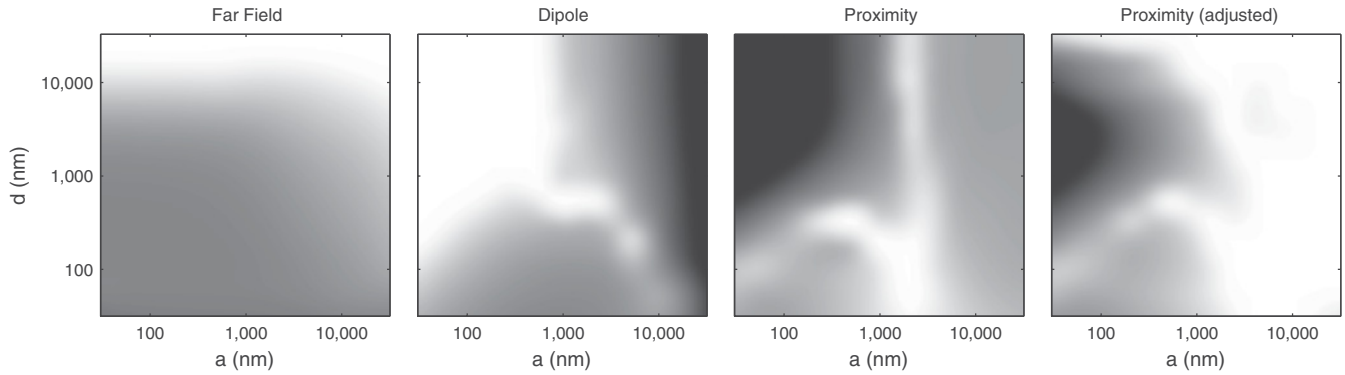
FIG. 6. A phase-space diagram of the relative accuracy of four approximations to the sphere-plate heat flux. The grayscale corresponds to the error as where corresponds to the far-field, dipole, proximity, or 'far-field adjusted' proximity approximations, respectively. The minimum error (corresponding to white) is 3%. The maximum error (corresponding to black) is 450%. The images are rendered from a smoothed interpolation of 147 data points.

by integrating, over all incidence angles, the absorption into the plate of far-field plane waves from the sphere. In general, the numerically exact Q deviates from Q_{ff} only when d is sufficiently small. The near-field contribution is significant only when $d \lesssim 1\ \mu$m (see Fig. 4, $d = 100$ nm, 1000 nm).

Perhaps somewhat surprisingly, our results reveal that for every gap size d, Q always approaches Q_{ff}, in the limit of large a. This is true even when the gap size is as small as $d = 100$ nm, when one might expect a substantial near-field contribution. This behavior arises from the specific geometric aspects of the sphere-plate configuration. When the gap size is small, the evanescent near-field component of the heat flux scales as a/d, according to the scaling arguments associated with the proximity approximation. On the other hand, the far-field component always scales with the area of the sphere $\propto a^2$, independent of gap size. Thus, given any gap size, the near-field component is negligible compared to the far-field component when the radius of the sphere is large enough. This observation is relevant for experimental design: In order to achieve substantial enhancement of heat flux above the far-field limit, it is important to use small, micrometer- (or submicrometer-) scale spheres, as can be inferred from Fig. 4.

Dipole approximation. In Fig. 4, Q_{dipole} is the result from the dipole approximation, which treats the sphere as a single-point dipole emitter.[30] Referring to Fig. 3, we find that for any given d, Q_{dipole} asymptotically approaches Q when $a \ll d$, and that the dipole approximation is actually quite good over a substantial range of radii. For example, when $d = 1\ \mu$m, Q_{dipole} deviates from Q by less than 10%, even for a as large as $a \approx d = 1\ \mu$m, and deviates only when $a > d$. Since the enhancement over the far-field limit is most prominent when the sphere is small, our results here indicate that the dipole approximation is useful in regimes where enhancement over the far-field limit is substantial.

Proximity approximation. In Fig. 4, Q_{prox} is the result from the proximity approximation,[14,31] which assumes that all heat transfer occurs pointwise, between the closest points on the sphere and plate. Mathematically,

$$Q_{\mathrm{prox}}(a,d) = \int_0^a dr\, 2\pi r\, Q_{pp}(d + a - \sqrt{a^2 - r^2}),\quad (17)$$

where $Q_{pp}(h)$ is the heat flux surface density for two plates separated by a distance h, which is known analytically.[1]

Referring again to Fig. 4, we observe that for small radii ($a \ll d$, a regime very relevant to enhancement over the far-field limit), the proximity approximation consistently overestimates the heat flux for two related reasons. First, it ignores the effect that the spherical curvature has on scattering. Second, it does not distinguish between propagating and evanescent waves. As recognized in the literature, the proximity approximation does provide a useful approximation when $a > d$. However, when $a \gg d$, the proximity approximation does not approach the correct far-field limit; it underestimates the far-field contribution due to emission by the part of the sphere far from the plate. Since it fails in both extremes of radius, it is difficult to interpret the physical meaning of the proximity approximation.

The proximity approximation is of practical use when $a \gg d$, though, if the prescription recommended in Ref. 32 is followed, whereby the far-field and near-field components are treated separately so that the correct far-field limit is attained. This is equivalent to adding a constant correction term to the unadjusted proximity approximation. If we compare the exact data to the adjusted proximity data for $a = 20\ \mu$m, by directly comparing the corresponding fit parameters in Eq. (16), we find that the parameters change by $\sim$1%. This agreement gets better as the sphere gets larger.

As another illustration, we plot in Fig. 5 the heat flux as a function of d for fixed $a = 1\ \mu$m. We notice that the proximity and dipole approximations are valid when $d < a$ and $d \gg a$, respectively. The crossover between the two regimes occurs near $d \approx 300$ nm; none of the standard approximations apply in this case.

Finally, to visually summarize the validity of these various approximations in different regimes, we present in Fig. 6 a regime map of the parameter space. Note again that while there is no limit in which the proximity approximation is valid, the far-field adjusted proximity approximation is valid in the large and large limits.

V. SUMMARY

We have presented a numerically exact and computationally efficient method for calculating the fluctuational electromagnetic heat transfer between a dielectric sphere and plate separated by nanoscale gaps. We described the physical principles, the mathematical formulation, and aspects of our computer implementation. We compared the results to existing experimental data, and to existing approximate methods.

While we have focused on the sphere-plate geometry, the method we have outlined can be generalized to other multiple-body geometries, provided the scattering matrix for each individual body is known. The underlying method is therefore of general applicability for understanding a variety of near-field electromagnetic effects, including Casimir effects, optical forces, and vacuum friction.[34,35]

APPENDIX

Here we provide the explicit formula for R, Λ, and A^0 in Eqs. (6)–(8).

The physically relevant solutions of the wave equation $(\nabla^2 + k^2)\Xi = 0$ can be written in spherical vector harmonics $\Xi \in \{\Psi_\alpha\}$ or in cylindrical vector harmonics $\Xi \in \{\Phi_\beta\}$:

$$\Psi_{\alpha(P=M)} = z_l^{(s)}(kr)\frac{1}{\sqrt{l(l+1)}}\left[\hat{\theta}\left(\frac{im}{\sin\theta}Y_l^m\right) + \hat{\phi}\left(-Y_l'^m\right)\right],$$

$$\Psi_{\alpha(P=N)} = \zeta_l^{(s)}(kr)\frac{1}{\sqrt{l(l+1)}}\left[\hat{\theta}\left(Y_l'^m\right) + \hat{\phi}\left(\frac{im}{\sin\theta}Y_l^m\right)\right] + \hat{\mathbf{r}}\left(\frac{z_l^{(s)}(kr)}{kr}\sqrt{l(l+1)}Y_l^m\right),$$

$$\Phi_{\beta(P=M)} = e^{ihz}e^{im\phi}\left[\hat{r}\left(i\frac{m}{r}J_m(\lambda r)\right) + \hat{\phi}[-\lambda J_m'(\lambda r)]\right],$$

$$\Phi_{\beta(P=N)} = e^{ihz}e^{im\phi}\left[\hat{r}\left(i\frac{h\lambda}{k}J_m'(\lambda r)\right) + \hat{\phi}\left(\frac{-hm}{kr}J_m(\lambda r)\right) + \hat{z}\left(\frac{\lambda^2}{k}J_m(\lambda r)\right)\right].$$

(A1)

Here, we denote the total wave number by k, the axial wave number by $h = k\cos\theta$, and the radial wave number by $\lambda = k\sin\theta$. J_m are the Bessel functions and Y_l^m are the spherical harmonics. Primed functions denote the first derivative of the function.

For a planar interface between two unbounded homogenous dielectric half-spaces, one is denoted by V_f (the background medium, typically free space) and the other by V_b (typically the substrate in near-field heat transfer experiments), the reflection coefficient for an axially propagating cylindrical wave incident on V_b from V_f is

$$R_{\beta\beta} = \delta_{\beta\beta}\left(\delta_{p\perp}\frac{h_f - h_b}{h_b + h_f} + \delta_{p\parallel}\frac{h_b(k_f/k_b) - h_f(k_b/k_f)}{h_b(k_f/k_b) + h_f(k_b/k_f)}\right).$$

(A2)

For a spherical region V_a consisting of a homogenous dielectric, embedded in an unbounded region V_f, the reflection coefficient at the interface for a spherical wave incident on V_a from V_f is[23]

$$R_{\alpha\alpha'} = \delta_{\alpha\alpha'}\left(\delta_{PM}\frac{k_a\zeta_l^{(1)}(k_a a)z_l^{(1)}(k_f a) - k_f\zeta_l^{(1)}(k_f a)z_l^{(1)}(k_a a)}{k_a\zeta_l^{(1)}(k_a a)z_l^{(3)}(k_f a) - k_f\zeta_l^{(3)}(k_f a)z_l^{(1)}(k_a a)} + \delta_{PN}\frac{k_a\zeta_l^{(1)}(k_f a)z_l^{(1)}(k_a a) - k_f\zeta_l^{(1)}(k_a a)z_l^{(1)}(k_f a)}{k_a\zeta_l^{(3)}(k_f a)z_l^{(1)}(k_a a) - k_f\zeta_l^{(1)}(k_a a)z_l^{(3)}(k_f a)}\right). \quad \text{(A3)}$$

Here, $z_l^{(1)}$ are the spherical Bessel functions, $z_l^{(3)}$ are the spherical Hankel functions, and $\zeta_l^{(s)}(x) = \frac{1}{x}\frac{d}{dx}[xz_l^{(s)}(x)]$. The transformation between cylindrical and spherical waves can be described by[25]

$$\Lambda_{\alpha\beta}\Phi_{\beta(mu)} = \sum_{l=m}^{\infty}\delta_{PM}\Psi_{\alpha(M)}ki^{l-m-1}\frac{(2l+1)(l-m)!}{l(l+1)(l+m)!}u^2 P_l'^m(\sqrt{1-u^2}) + \delta_{PN}\Psi_{\alpha(N)}ki^{l-m-2}\frac{m(2l+1)(l-m)!}{l(l+1)(l+m)!}P_l^m(\sqrt{1-u^2}),$$

$$\Lambda_{\beta\alpha}\Psi_{\alpha(ml)} = \int_0^{\infty}du\frac{u}{\sqrt{1-u^2}}\left\{\delta_{PM}\Phi_{\beta(M)}\frac{1}{2k}i^{m-l+1}P_l'^m(\sqrt{1-u^2}) + \delta_{PN}\Phi_{\beta(N)}\frac{m}{2ku^2}i^{m-l-1}P_l^m(\sqrt{1-u^2})\right\}.$$

(A4)

Here, $u = \sin\theta$ and P_l^m is the associated Legendre polynomial of degree l and order m. Note that Eq. (A4) includes contributions from evanescent waves, for which $u > 1$, and thus differs from Ref. 25, which includes only propagating waves with $0 \leqslant u \leqslant 1$.

The numerical behavior of certain special functions for large orders and degrees is of practical importance. In particular, $1/j_l$, h_l, and P_l^m diverge for large l, so it is useful, from a numerical standpoint, to instead calculate renormalized functions $\{e^{ihz}P_l^m j_l, e^{ihz}P_l'^m j_l, e^{ihz}P_l^m/h_l, e^{ihz}P_l'^m/h_l\}$. These routines have been efficiently implemented with recursive $C++$ functions,[28] and are evaluated within numerical

quadrature routines for calculating $T_{\alpha_+\alpha_+'}$ in Eq. (8) and $S_{\alpha_+\alpha_+'}$ in Eq. (12). The complete formulas for $T_{\alpha_+\alpha_+'}$ and $S_{\alpha_+\alpha_+'}$ are lengthy, but can be found in the source code.[28]

Finally, the thermal emission of an isolated sphere is given by[23]

$$A_{\alpha(l,P=M)}^0 = \frac{-i/(k_f a)}{k_a \zeta_l^{(1)}(k_a a) z_l^{(3)}(k_f a) - k_f \zeta_l^{(3)}(k_f a) z_l^{(1)}(k_a a)}$$

$$A_{\alpha(l,P=N)}^0 = \frac{i/(k_f a)}{k_a \zeta_l^{(3)}(k_f a) z_l^{(1)}(k_a a) - k_f \zeta_l^{(1)}(k_a a) z_l^{(3)}(k_f a)}.$$

$$(A5)$$

[1] D. Polder and M. van Hove, Phys. Rev. B **4**, 3303 (1971).

[2] C. M. Hargreaves, Phys. Lett. A **30**, 491 (1969).

[3] J. B. Xu, K. Läuger, R. Moller, K. Dransfeld, and I. H. J. Wilson, Appl. Phys. **76**, 7209 (1994).

[4] S. Basu, Z. M. Zhang, and C. J. Fu, Int. J. Energy Res. **33**, 1203 (2009).

[5] J. L. Pan, H. K. Choy, and C. G. Fonstad, IEEE Trans. Electron Devices **47**, 1 (2000).

[6] B. J. Lee, Y.-B. Chen, and Z. M. Zhang, J. Quant. Spectrosc. Radiat. Transf. **109**, 608 (2008).

[7] A. Kittel, U. F. Wischnath, J. Welker, O. Huth, F. Rüting, and S.-A. Biehs, Appl. Phys. Lett **93**, 193109 (2008).

[8] Y. De Wilde, F. Formanek, R. Carminati, B. Gralak, P.-A. Lemoine, K. Joulain, J.-P. Mulet, Y. Chen, and J. J. Greffet, Nature (London) **444**, 740 (2006).

[9] U. F. Wischnath, J. Welker, M. Munzel, and A. Kittel, Rev. Sci. Instrum. **79**, 073708 (2008).

[10] A. Kittel, W. Müller-Hirsch, J. Parisi, S.-A. Biehs, D. Reddig, and M. Holthaus, Phys. Rev. Lett. **95**, 224301 (2005).

[11] W. A. Challener, C. Peng, A. V. Itagi, D. Karns, W. Peng, Y. Peng, X. Yang, X. Zhu, N. J. Gokemeijer, Y.-T. Hsia, G. Ju, R. E. Rottmayer, M. A. Seigler, and E. C. Gage, Nat. Photonics **3**, 220 (2009).

[12] A. Narayanaswamy, S. Shen, and G. Chen, Phys. Rev. B **78**, 115303 (2009).

[13] S. Shen, A. Narayanaswamy, and G. Chen, Nano Lett. **9**, 2909 (2009).

[14] E. Rousseau, A. Siria, G. Jourdan, S. Volz, F. Comin, J. Chevrier, and J. J. Greffet, Nat. Photonics **3**, 514 (2009).

[15] M. Krüger, T. Emig, and M. Kardar, Phys. Rev. Lett. **106**, 210404 (2011).

[16] C. Otey and S. Fan, e-print arXiv:1103.2668 (to be published).

[17] A. P. McCauley, M. T. H. Reid, M. Krüger, and S. Johnson, e-print arXiv:1107.2111 (to be published).

[18] S. J. Rahi, T. Emig, N. Graham, R. L. Jaffe, and M. Kardar, Phys. Rev. D **80**, 085021 (2009).

[19] A. Canaguier-Durand, P. A. M. Neto, A. Lambrecht, and S. Reynaud, Phys. Rev. A **82**, 012511 (2010).

[20] R. Messina and M. Antezza, e-print arXiv:1012.5183 (to be published).

[21] S. M. Rytov, *Theory of Electric Fluctuations and Thermal Radiation* (Air Force Cambridge Research Center, Bedford, MA, 1959).

[22] K. Joulain, J.-P. Mulet, F. Marquier, R. Carminati, and J. J. Greffet, Surf. Sci. Rep. **57**, 59 (2005).

[23] A. Narayanaswamy and G. Chen, Phys. Rev. B **77**, 075125 (2008).

[24] P. Lax and R. Phillips, *Scattering Theory* (Academic, New York, 1967).

[25] G. Han, Y. Han, and H. J. Zhang, J. Opt. A, Pure Appl. Opt. **10**, 015006 (2008).

[26] W. H. Press, S. A. Teukolsky, W. T. Vetterling, and B. P. Flannery, *Numerical Recipes in C: The Art of Scientific Computing*, 2nd ed. (Cambridge University Press, New York, 1992).

[27] E. D. Palik, *Handbook of Optical Constants of Solids* (Elsevier, New York, 1998).

[28] See [http://www.stanford.edu/group/fan/shs].

[29] A. I. Volokitin and B. N. J. Persson, Phys. Rev. B **63**, 205404 (2001).

[30] J. P. Mulet, K. Joulain, R. Carminati, and J. J. Greffet, Appl. Phys. Lett. **78**, 2931 (2001).

[31] S. A. Biehs and J. J. Greffet, Phys. Rev. B **81**, 245414 (2010).

[32] K. Sasihithlu and A. Narayanaswamy, Phys. Rev. B **83**, 161406 (2011).

[33] B. V. Derjaguin, I. I. Abrikosova, and E. M. Lifshitz, Q. Rev., Chem. Soc. **10**, 295 (1956).

[34] A. I. Volokitin and B. N. J. Persson, Rev. Mod. Phys. **79**, 1291 (2007).

[35] P. A. M. Neto, A. Lambrecht, and S. Reynaud, Phys. Rev. A **78**, 012115 (2008).